Nano and picosecond magnetization dynamics of weakly coupled CoFe/Cr/NiFe trilayers studied by a multitechnique approach

A. M. Kaiser, ¹ C. Schöppner, ² F. M. Römer, ² C. Hassel, ² C. Wiemann, ¹ S. Cramm, ¹ F. Nickel, ¹ P. Grychtol, ¹ C. Tieg, ^{3,*} J. Lindner, ² and C. M. Schneider ^{1,4}

¹Peter-Grünberg-Institut PGI-6, Forschungszentrum Jülich and JARA-FIT, DE-52425 Jülich, Germany ²Fachbereich Physik and Center for Nanointegration (CeNIDE), AG Farle, Universität Duisburg-Essen, Lotharstr. 1, DE-47048 Duisburg, Germany

³European Synchrotron Radiation Faclity ESRF, FR-38043 Grenoble, Cedex, France ⁴Fakultät f. Physik and center for Nanointegration (CeNIDE), AG NanoSync, Universität Duisburg-Essen, Lotharstr. 1, DE-47048 Duisburg, Germany

(Received 16 May 2011; published 10 October 2011)

We present results on the magnetization dynamics in heterostructures of the CoFe/Cr/NiFe type. We have employed a combination of different layer-selective methods covering a broad range from quasistatic hysteresis measurements by x-ray magnetic circular dichroism (XMCD), over time-resolved photoemission electron microscopy (PEEM) at subnanosecond timescales to high-frequency ferromagnetic resonance (FMR) experiments. With increasing driving frequency, we found a different influence of the coupling between the two ferromagnetic layers on the dynamic behavior. Employing the spatial resolution of the PEEM method, we have been able to discern various dynamic responses in different regions of the sample that could be attributed to magnetodynamic processes with a different degree of coupling. In conjunction with the complementary FMR and XMCD measurements, we attribute the inhomogeneous influence of interlayer coupling to a shift from domain-wall-motion-dominated dynamics at low frequencies to precession-dominated dynamics at higher frequencies.

DOI: 10.1103/PhysRevB.84.134406 PACS number(s): 75.78.-n, 68.37.Xy, 76.50.+g

I. INTRODUCTION

The physics governing magnetization reversal and switching phenomena has been a matter of intense research for more than hundred years. Soon it became clear that a variety of dynamic processes on different time scales are involved in magnetization reversal such as domain-wall motion, coherent precession, or the excitation of spin-wave modes. Nowadays, we have arrived at a quite detailed understanding of the magnetization dynamics down to the picosecond time scale, particularly, in single thin film elements. This is to a large extent also due to the development of reliable micromagnetic simulations on the basis of the Landau-Lifshitz-Gilbert (LLG) formalism.^{2,3} The improvement of our knowledge of the microscopic mechanisms determining magnetization dynamics is closely connected to the evolution of magnetic recording technology, enabling more reliable and faster write and read procedures. Modern magnetic storage devices such as hard disks read heads⁴ or MRAM cells,⁵ however, are comprising complex layer stacks with a sophisticated magnetic architecture. As a consequence, a thorough description of the dynamics occurring in these systems poses challenges for both experimental characterization and simulation. On the one hand, the situation asks for an additional important feature of the measurement technique: the discrimination of the magnetic dynamics of individual layers. This is a prerequisite to disentangle the influence of coupling effects between adjacent layers such as exchange interlayer coupling⁶ or exchange anisotropy^{7,8} on the dynamic behavior. On the other hand, these coupling effects have to be appropriately taken into account also into the micromagnetic simulations.

A powerful tool for carrying out layer-resolved experiments with magnetic sensitivity is x-ray magnetic circular/linear

dichroism (XMCD/XMLD). ^{9,10} Using a pump-probe approach based on pulsed synchrotron radiation, this method has become a commonly used technique for the study of magnetization dynamics. The experiments can be performed both spatially integrated ¹¹ and laterally resolved by using photoemission electron microscopy (PEEM) ^{12,13} or x-ray microscopy. ¹⁴ Depending on the pulse width of the synchrotron radiation, the time resolution of this time-domain approach may range down into the 10-picosecond regime.

Another important and complementary tool for the study of magnetization dynamics in the high-frequency domain is ferromagnetic resonance (FMR). Although FMR is not an element-specific method, it allows one to separate the response of magnetic layers within a heterostructure, as long as they differ in their magnetic properties such as saturation magnetizations or magnetic anisotropies. This allows for the assignment of different resonance peaks in a multilayer spectrum to those originating from the individual single layers. Moreover, it is possible to derive the influence of interlayer coupling on the measured resonance spectra by comparing the experimental data with theoretical simulations. ^{16,17}

We have employed a combination of three techniques to study the magnetization dynamics of weakly coupled CoFe/Cr/NiFe trilayers over a broad range of excitation frequencies from quasistatic (~0 Hz) magnetization reversal (using spatially integrated XMCD measurements) up to magnetodynamics in the 10-GHz range (using FMR measurements). The intermediate range (~1 GHz) was covered by time-resolved PEEM experiments with excitations in the nanosecond regime. Using the spatially resolving PEEM technique, the temporal characteristics of different reversal processes such as magnetization rotation, domain-wall motion

and domain nucleation can be discriminated in both layers and the complex magnetic behavior is found to be strongly inhomogeneous, depending on the local effective magnetic field consisting of different contributions (demagnetizing field, external field, and interlayer coupling). Using the elemental discrimination of x-ray excited PEEM, we have been able to study the individual response of both magnetic constituents of a trilayer system, as described in Ref. 18.

II. EXPERIMENTAL DETAILS

A thin film stack of Ni₈₀Fe₂₀(2 nm)/Cr(2.5 nm)/ Co₅₀Fe₅₀(5 nm) was grown on epitaxial Ag coplanar waveguides, which have been deposited onto GaAs(001) substrates with a 1-nm Fe seed layer by means of molecular beam epitaxy. 19 The epitaxial growth of the films has been confirmed by in situ LEED measurements during the film deposition indicating bcc growth of the CoFe film. The XMCD and FMR measurements have been carried out on extended films, while for the PEEM measurements, the films have been microstructured by optical lithography and Ar ion beam milling. This lead to a defined ground-state domain configuration due to the demagnetizing field emanating from the edges of the microstructures. The films were capped by a 2-nm Au film serving as oxidation protection. Prior to the measurements, the samples have been demagnetized in an oscillating magnetic field in order to obtain a ground-state domain structure. The NiFe/Cr/CoFe system is interlayer-exchange coupled via the Cr interlayer. The sign and magnitude of the coupling depends on the Cr interlayer thickness in an oscillatory manner. ^{20–22} For the studied case of 2.5 nm Cr thickness, the two ferromagnetic films are weakly coupled and the layer magnetizations align parallel.

The microscopy experiments employed an electrostatic photoemission electron microscope based on the FOCUS IS-PEEM design.²³ It was installed at the beamline ID08 at the ESRF (Grenoble, France) providing circularly polarized soft x rays. The storage ring was operated in the 16-bunch mode, resulting in a pulse repetition period of 176 ns at a light pulse width of about 50 ps. By exploiting the pulsed structure of the synchrotron light, we conducted pump-probe experiments of the magnetization dynamics. Magnetic excitation was achieved by passing short current pulses down the coplanar waveguides, thereby creating a magnetic Oersted field acting on the magnetic elements fabricated on top of the waveguide. The current pulses are synchronized to the x-ray pulses via an electronic delay generator allowing for an adjustable delay between pump (magnetic field) and probe (x-ray) pulses.

The XMCD measurements have been conducted in a dedicated chamber mounted at the beamline UE56/1-SGM at BESSY II. The experimental setup allows for measurements with an in-plane rotatable magnetic field of up to 0.5 T. The measurements have been carried out in grazing incidence by measuring the sample current while varying the magnetic field in beam direction. The hysteresis loops have been generated by calculating the XMCD asymmetry

$$A_{\text{XMCD}} = \frac{I_{\sigma+} - I_{\sigma-}}{I_{\sigma+} + I_{\sigma-}} \tag{1}$$

with $I_{\sigma\pm}$ denoting the intensity measured with illumination of right $(\sigma+)$ and left $(\sigma-)$ circularly polarized light, re-

spectively. By tuning the photon energy to the corresponding absorption edges, these measurements can be carried out in an elementally resolved way allowing for layer-selective measurements in a heterostructure system.

Ferromagnetic resonance (FMR) spectra were recorded at a microwave frequency of 9.85 GHz as a function of the azimuthal in-plane angle of the external magnetic field at room temperature. In a homogeneously magnetized ferromagnetic thin film of cubic symmetry, the free energy density F includes the Zeeman energy, demagnetizing energy, the perpendicular uniaxial $K_{2\perp}$ as well as the cubic K_4 anisotropy energy density:

$$F = -MB[\sin\theta\sin\theta_B\cos(\phi - \phi_B) + \cos\theta\cos\theta_B]$$

$$-\left(\frac{1}{2}\mu_0M^2 - K_{2\perp}\right)\cos^2\theta + K_{2\parallel}\sin^2\theta\cos^2(\phi - \delta)$$

$$+ K_4\sin^2\theta - \frac{K_4}{8}(7 + \cos 4\phi)\sin^4\theta. \tag{2}$$

Here, $\theta_{\rm B}(\theta)$ and $\phi_{\rm B}(\phi)$ are the polar and azimuthal angles of the external field \vec{B} (magnetization \vec{M}) with respect to the out-of-plane [001]- and in-plane [100] directions. In order to take into account uniaxial in-plane anisotropy that might originate from the interfaces, the term being proportional to $K_{2\parallel}$ was introduced. δ is the angle defining the principal direction of the in-plane uniaxial anisotropy with respect to the [100] direction. According to the Smit and Beljers approach, ²⁴ the resonance condition in an FMR experiment for the in-plane configuration $(\theta_B = \theta = \pi/2)$ becomes

$$\left(\frac{\omega}{\gamma}\right)^{2} = \left[B_{\text{res}}\cos\Delta\phi - \mu_{0}M_{\text{eff}} + \frac{K_{4}}{2M}(3 + \cos 4\phi_{\text{eq}}) + \frac{2K_{2\parallel}}{M}\cos^{2}(\phi_{\text{eq}} - \delta)\right] \left[B_{\text{res}}\cos\Delta\phi + \frac{2K_{4}}{M}\right] \times \cos 4\phi_{\text{eq}} + \frac{2K_{2\parallel}}{M} \times \cos 2(\phi_{\text{eq}} - \delta)\right], \quad (3)$$

where $\Delta \phi = \phi_{\rm eq} - \phi_{\rm B}$, $\phi_{\rm eq}$ is the equilibrium angle of magnetization, and $B_{\rm res}$ is the resonance field in the in-plane geometry. $\mu_0 M_{\rm eff} = \frac{2K_{2\perp}}{M} - \mu_0 M$ denotes the effective out-of-plane anisotropy field including a contribution due to the shape anisotropy and an intrinsic contribution given by $\frac{2K_{2\perp}}{M}$. $\gamma = g\mu_B/\hbar$ (g is the g factor) is the gyromagnetic ratio.

III. QUASISTATIC HYSTERESIS LOOPS

The quasistatic switching behavior of the CoFe and NiFe layers has been studied by XMCD measurements. Element-selective measurements have been carried out with the photon energy tuned to the appropriate absorption edges (CoFe: Co-L₃, NiFe: Ni-L₃). The hysteresis measurements are shown in Fig. 1 for (a) the single layered samples CoFe/Ag and NiFe/Ag and (b) the individual layers of a trilayer sample incorporating a 2.5-nm-thick Cr interlayer. While the single layers show distinctly different switching fields, the situation changes drastically in the trilayer system: the coercive fields of both layers shift to the same value H_c due to the coupling of both layers favoring a parallel alignment. However, the measurements show a slight rotation of the NiFe magnetization relative to the CoFe magnetization for $H < H_c$. Using SQUID

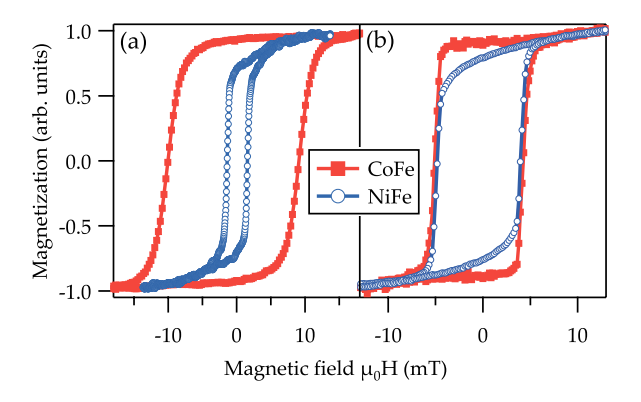


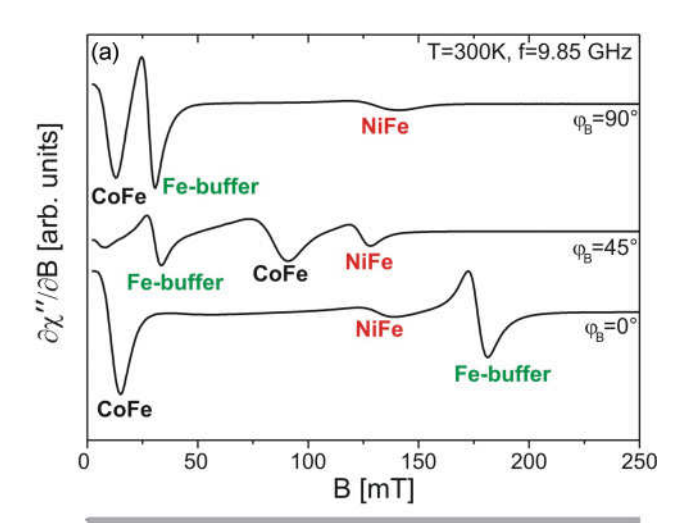
FIG. 1. (Color online) Layer-resolved hysteresis loops of 5-nm CoFe and 2-nm NiFe for (a) single layered films and (b) parts of a trilayer sample incorporating a 2.5-nm-thick Cr interlayer.

magnetometry, the saturation magnetization of both layers has been derived as $\mu_0 M_s^{\text{NiFe}} = 1 \text{ T}$ and $\mu_0 M_s^{\text{CoFe}} = 2.16 \text{ T}$.

IV. HIGH-FREQUENCY FERROMAGNETIC RESONANCE

The FMR measurements have been carried out both on single CoFe and NiFe films and parallel coupled trilayer films. Figure 2(a) shows FMR spectra of the trilayer recorded at a microwave frequency of v = 9.85 GHz with the external magnetic field oriented along three different directions in the film plane. One can identify three different resonances that all show a pronounced dependence on the in-plane angle $\phi_{\rm B}$. Figure 2(b) shows the FMR in-plane angular dependence in the range $0 \le \phi_B \le 270^\circ$. The grey scale plot with the color markings indicating the magnitude of the FMR signal (white corresponding to positive and black to negative signals) shows all spectra with the angle ϕ_B given on the x axis and the magnetic induction B on the y axis. It has to be noted that due to lock-in detection, the derivative of the absorption signal with respect to the magnetic field is measured [see also Fig. 2(a)]. The absorption signal corresponds to the imaginary part of the high-frequency susceptibility χ'' . A signal is thus given by a change of color between white and black.

The full angular dependence provided by the grey level plot reveals that the three signals follow a different angular dependent behavior. By fitting the data one can extract the anisotropy fields (compiled in Table I) corresponding to the three signals that can be identified by comparison with the single-layer spectra. This result allows us to draw the following conclusions: (i) the signal of the 1-nm-thick Fe seed layer (dashed green line) yields a dominating twofold symmetry and a smaller cubic contribution. Such behavior of thin Fe layers on GaAs(001) has been reported in previous experiments²⁵ where the twofold anisotropy contribution has been attributed to surface reconstructions of the GaAs(001) substrates. (ii) The CoFe bottom layer (dashed black line) exhibits a fourfold anisotropy, too, resulting very likely from the epitaxial growth on the Ag(001) buffer layer. The easy-axis direction corresponds to the [110] direction of bcc CoFe and is rotated by 45° with respect to the one of bcc Fe, as determined by reference measurements and previous studies.²⁶ The overall shift of the angular dependence of the CoFe data with respect to the NiFe data toward smaller resonance fields supports



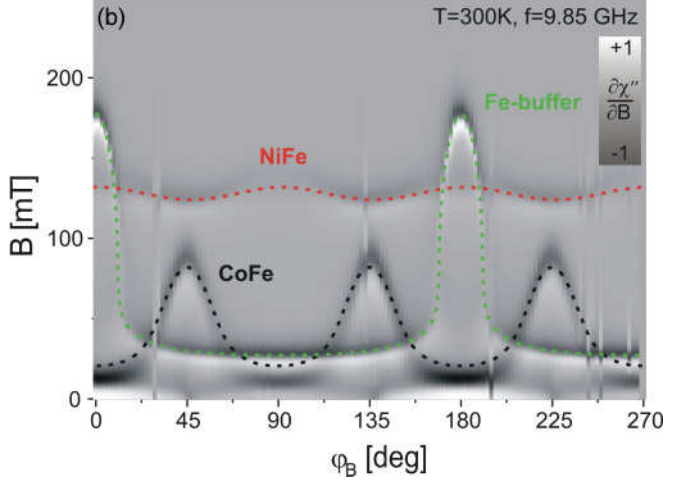


FIG. 2. (Color online) FMR measurements on CoFe/Cr/NiFe trilayer: (a) FMR spectra at three in-plane angles and (b) in-plane angular dependence of the FMR signal. $\phi_B = 0$ corresponds to measurements along the [110] direction of the GaAs substrate and the CoFe films, for $\phi_B = 45^\circ$, the field is directed toward the [010] direction.

the finding of a higher magnetization of CoFe than NiFe. (iii) The NiFe top layer (dashed red line) shows a small angular variation. It is, however, interesting to note that the NiFe layer exhibits a weak fourfold anisotropy in the film plane, which may by caused by some residual epitaxial relationship to the underlying CoFe and Cr layers.

We note that the fits to the FMR measurements have been carried out both assuming coupled and uncoupled layers. It has been found that best fits were achieved by using no or

TABLE I. The magnetic anisotropy fields $\mu_0 M_{\rm eff}$ (effective out-of-plane anisotropy), $2K_4/M$ (cubic anisotropy), and $2K_{2\parallel}/M$ (uniaxial in-plane anisotropy) of the different layers extracted from the fits to the FMR data. The error is 5%.

Layer	$\mu_0 M_{\rm eff}$ (T)	$2K_4/M$ (mT)	$2K_{2\parallel}/M~(\text{mT})$
Fe-buffer	-1.36	23	77
CoFe	-2.26	35	0
NiFe	-0.86	4	0

very small interlayer coupling. This is supported by comparing the NiFe and CoFe layers, which exhibit opposite behavior with respect to hard and easy directions (i.e., high and small resonance fields, respectively). Consequently, one concludes that the system is governed by the anisotropy fields rather than by interlayer coupling. However, the fit quality was not significantly affected by including a coupling term that is smaller than 5% of the anisotropy fields. This value therefore provides a limiting upper value for the strength of the coupling field $\mu_0 H_{\text{coupl}} = J/(M_s t)$. Since M_{eff} is a contribution, which is isotropic within the film plane, only the anisotropic contributions $2K_{2\parallel}/M$ and the cubic anisotropy $2K_4/M$ play a role in this context. Using the largest in-plane anisotropy field obtained for the CoFe layer (its cubic anisotropy field, see Table I), one estimates $\mu_0 H_{\rm coupl}^{\rm CoFe} < 1.75$ mT corresponding to a weak influence of the coupling compared to other field components.

In order to investigate also the magnetic damping in the CoFe and NiFe layers, we have performed frequency-dependent FMR measurements. For this purpose, a method employing a semirigid microwave cable has been used. The cable is shorted at its end to generate microwaves of variable frequencies (details of this method are described elsewhere). The FMR linewidth ΔB_{pp} can be phenomenologically described by the Gilbert damping. This ansatz—neglecting other damping contributions—predicts the linewidth to scale linearly with the microwave frequency. It is given by

$$\Delta B_{pp} = \frac{2}{\sqrt{3}} \frac{2\pi \nu G}{\gamma^2 M},\tag{4}$$

Here, G is the phenomenological Gilbert parameter that has the unit Hz. It is linked to the widely used dimensionless damping constant by $\alpha = G/(\gamma M)$. One should note that this relationship only holds for a situation in which the external magnetic field and magnetization are aligned parallel to each other. To ensure this, we have measured along principal directions of the system, i.e., along minima or maxima of the angular dependence shown in Fig. 2(b). Along either easy or hard directions, the equilibrium angle of the magnetization is aligned parallel to the external field. Figure 3, where the measurements in the frequency range 12–18 GHz together with fits to Eq. (3) are plotted, clearly shows that the damping parameter α of the CoFe layer is about a factor of four smaller than the one of the NiFe layer.

V. SPATIALLY RESOLVING MEASUREMENTS

Spatially resolved magnetization dynamics has been investigated by XMCD-PEEM. XMCD images have been acquired by taking pictures of the lateral distribution of the photoexcited electrons with illumination of left and right circularly polarized x rays and the photon energy tuned to the appropriate absorption edge and calculating the XMCD asymmetry $A_{\rm XMCD}$ according to Eq. (1) for each single pixel. Thus the grey values of each pixel correspond to the projection of the local magnetization direction $\mathbf{M}(\mathbf{r})$ on the light incidence direction \mathbf{q} : $A_{\rm XMCD}(\mathbf{r}) \propto \cos(\alpha)$, where α is the angle between $\mathbf{M}(\mathbf{r})$ and \mathbf{q} .

The sample has been excited by Gaussian-shaped field pulses with FWHM = 600 ps and a magnetic field amplitude

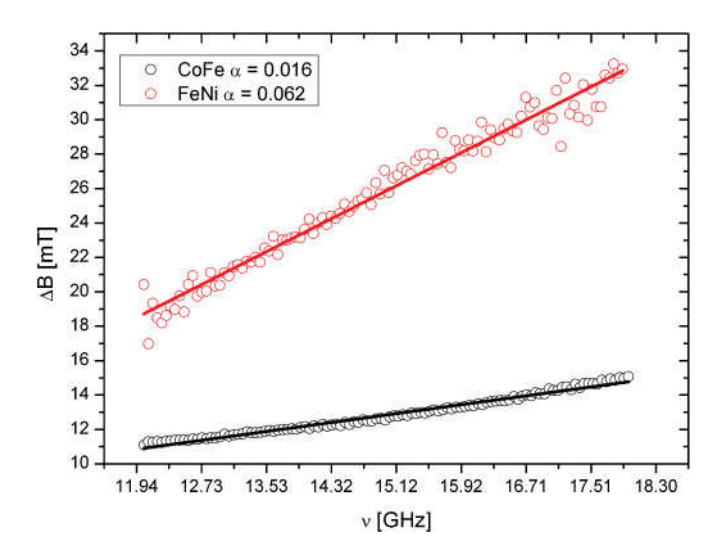


FIG. 3. (Color online) Peak-to-peak FMR linewidth (ΔB_{pp}) as a function of the frequency for CoFe (black circles) and NiFe (red circles). The experimental error of this method for determining α is $\Delta \alpha = 0.01$.

of 5 mT. The repetitive pump-probe measurement principle is limited to imaging of reversible processes, i.e., after each cycle, the system has to reliably return to the same micromagnetic starting configuration (domain pattern). Usually this is the configuration achieved by the demagnetization process described above. In contrast to our earlier studies on single Permalloy thin film elements (see e.g., Ref. 28), however, the magnetization configuration of the trilayer system revealed a strong tendency to get trapped into one of a variety of metastable states when the excitation employed unipolar field pulses. Obviously, the restoring force provided by the demagnetizing field was not sufficient to reliably reach the ground state during all pump-probe cycles. This preference for metastable states may be due to the interlayer coupling, which introduces an additional contribution to the local and global energy balance.

In an effort to overcome this problem, we therefore excited the system with bipolar pulses. Indeed, the second, somewhat smaller pulse of opposite polarity was found to release the system from any metastable state and to reliably restore the ground-state configuration after each pump-probe cycle. Images showing the individual magnetization distribution of each layer for subsequent pump-probe delays are compiled in Fig. 4. The ground-state magnetization configuration is indicated by the black and white arrows revealing a domain pattern similar to the characteristic Landau pattern consisting of four triangular domains magnetized parallel to the element edges.²⁹ The equilibrium configuration is similar for both layers and is determined by the need of the magnetic system to reach the lowest total energy state in the presence of a parallel interlayer exchange coupling. It has to be noted that the system is additionally influenced by defects on the surface (visible as dark spots in the images) and the periodic excitation of the system. Therefore the magnetization configuration deviates slightly from the Landau state by forming slightly bent domain walls even in the initial state.

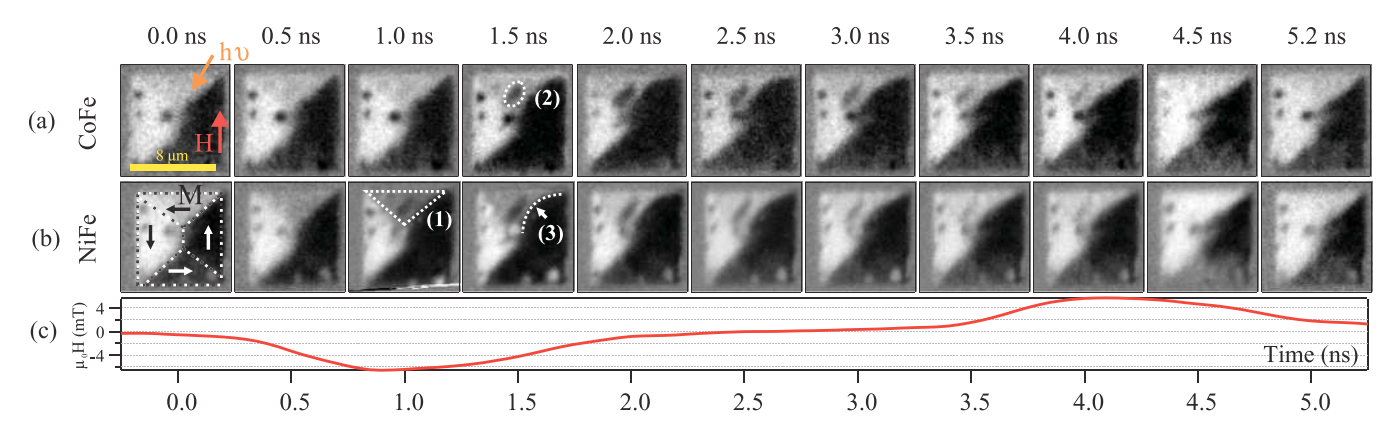


FIG. 4. (Color online) XMCD images of the layer-resolved magnetization dynamics. (a) Response of the CoFe layer measured at the Co- L_3 edge, (b) response of the NiFe layer measured at the Ni- L_3 edge, and (c) temporal profile of the excitation pulse. The light-incidence and positive magnetic field directions are indicated by the arrows marked with $h\nu$ and H, respectively. The domain configuration in the ground state is marked by the black and white arrows and the black-white dashed lines are marking the domain walls. The numbers (1)–(3) mark positions where magnetization rotation (1), domain nucleation (2), and domain-wall rotation (3) are observed.

Both films show qualitatively the same dynamical behavior with rich details. We have identified three regions RX where distinct micromagnetic processes on different time scales occur: (R1) magnetization rotation in the top and bottom domains toward the direction of the effective field, (R2) fast nucleation of an additional domain seen as a dark spot in the top triangle, and (R3) domain-wall motion perpendicular to the domain wall increasing the area of domains with the preferential magnetization direction parallel to the field. It has to be noted that in an ideal film system no nucleation of additional domains would be expected under the conditions present in our experiment. Thus we assume that this effect observed here can be primarily attributed to the presence of defects in our system at which the new domain nucleates. However, we do not expect that the low number of defects affects the general significance of our observations in terms of magnetization rotation and motion.

For all three processes, the largest changes are observed near the maxima of the magnetic field pulse train. However, a more careful examination of the images reveals different amplitudes and a slight phase shift of the magnetization rotation in both layers. This effect can be visualized by extracting the temporal variation of the magnetization direction from the images. Using the relation $A_{\rm XMCD} \propto \cos(\alpha)$, the angle between light incidence direction and magnetization can be derived from the local XMCD values. Figure 5 displays the results for the top and the bottom ferromagnetic layer for three different regions in which one of the processes (R1) to (R3) dominates. Note that the term "magnetization rotation" in the figure refers to an angular change in the local magnetization direction integrated over the small regions (R1-3), even if the underlying mechanism is a domain-wall motion or nucleation event. The advantage of this representation is a direct comparison of the dynamics resulting from different processes. It is particularly striking that the response of both layers is not synchronous, although they are coupled parallel in the static case. Instead, each micromagnetic process exhibits an individual dynamic signature that will be discussed in the following. (1) The largest difference appears for the genuine magnetization rotation (R1) in the topmost triangular domain, with the NiFe rotation angle being about twice as high as the CoFe rotation. Furthermore, the CoFe magnetization responds slower to magnetic field changes than the NiFe magnetization both during the rising and falling edge of the pulse. The first maxima are shifted with respect to each other by 250 ± 50 ps. Between the two field maxima the magnetization directions of the top and bottom layer are no longer collinear and include an angle of $7 \pm 2^{\circ}$. (2) Evaluating the area (R2), which is connected to a nucleation event, the difference in amplitude of magnetization

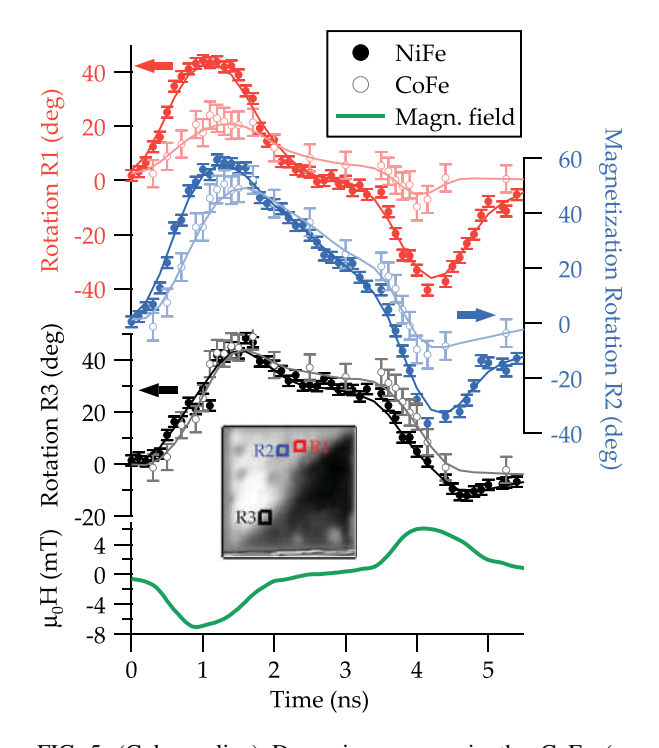


FIG. 5. (Color online) Dynamic response in the CoFe (open symbols) and NiFe layer (closed symbols) measured in three regions of interest of the $8\times 8~\mu m^2$ magnetic microstructure (marked in the inset) reproducing the temporal characteristics of magnetization rotation (R1), domain nucleation (R2), and domain-wall motion (R3). The lines provide a guide to the eye (data offset for clarity).

rotation in the two layers is less pronounced. However, the NiFe magnetization still exhibits a faster response to the rising edge of the pulse. (3) The temporal rotation profiles taken at the domain-wall position (R3) agree within the error bars, i.e., both walls move in a coupled manner. In both layers the first field pulse pushes the domain wall out of its equilibrium position. With the decay of the first field pulse a slow relaxation sets in. Only the second pulse of opposite field direction, however, restores the position of the domain wall. This illustrates the above argument about the metastable states. The synchronous wall motion in both layers is also confirmed by extracting the domain-wall position from line profiles perpendicular to the wall as demonstrated in Fig. 6. The maximum wall displacement is of the order of 800 nm.

What is the origin of the different switching or magnetization rotation speeds in the top and bottom layers? As a first step toward a more quantitative understanding, we adapt an empirical model introduced by Doyle, 30 which relates the switching time τ to the switching field H_0 :

$$\tau^{-1} = S_W^{-1}(H - H_0) \tag{5}$$

with the switching coefficient $S_W \propto 1/\alpha$ for the magnetization precession and a damping coefficient α < 0.1. Thus two different parameters may be relevant for the layer-dependent reaction times: the difference in the intrinsic switching fields H_0 and the damping parameters α of both layers. Although the XMCD measurements revealed simultaneous switching of both ferromagnetic layers, H_0 is a material-dependent parameter related to the single film coercive fields 11 and, therefore, it is distinctly higher for CoFe than for NiFe. In addition, the FMR measurements showed that $\alpha_{NiFe} > \alpha_{CoFe}$. Thus, if we take the material-dependent values of H_0 and α into account, we should expect a faster response in NiFe due to $\tau_{\text{NiFe}} < \tau_{\text{CoFe}}.$ This trend is in line with our experimental observations. It is important to note, however, that due to the incomplete magnetization switching—the pulse excitation does not lead to a full magnetization reversal—this relation can only serve as a qualitative guide rather than yielding a detailed analysis of the switching behavior.

Nevertheless, even taking into account material-dependent switching times, a strongly coupled trilayer system should

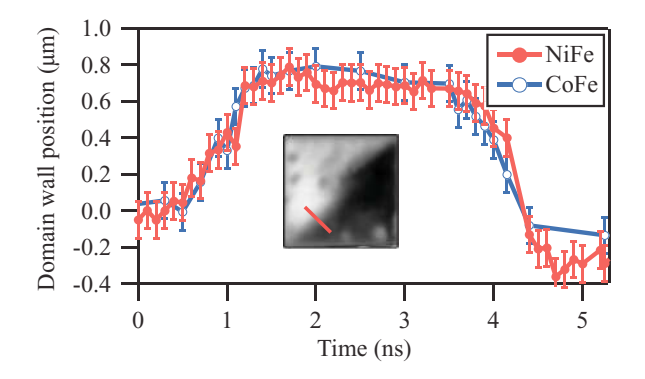


FIG. 6. (Color online) Time-resolved displacement of the domain wall measured along the red line (inset) under the influence of the bipolar magnetic field pulse with ± 5 mT amplitude. In both layers (closed symbols: NiFe, open symbols: CoFe) the domain-wall motion is synchronous.

not be expected to develop a significant canting of up to $7\pm2^\circ$ of the magnetization directions in the top and bottom layer. Obviously, the assumption of a magnetically stiff system does not apply in this case. From the static XMCD-PEEM investigations (not shown here) we know, that at a Cr interlayer thickness of 2.5 nm we are beyond the first antiferromagnetic coupling maximum, i.e., the system is weakly ferromagnetically coupled. Thus we can conclude that the temporal profile of the magnetization rotation is dominated by the material-dependent switching times with only marginal influence of the interlayer exchange coupling.

It should be pointed out, however, that such a "decoupled" behavior is not observed with respect to the domain-wall displacement. This seeming discrepancy can be understood by taking into account an additional interaction term in the effective field, which is related to the stray fields emanating from a domain wall.³¹ Locally, this field contribution enhances the effective coupling between the top and bottom layers and forces the domain walls in the two layers to move in unison.³² A similar situation arises close to the newly nucleated domain: during the leading edge of the magnetic field pulse, the NiFe magnetization is rotated without any delay while the CoFe rotation is lagging behind. However, when a certain threshold is overcome, the new domain is nucleated. This nucleation creates additional domain boundaries together with their stray fields. These fields again enhance the local coupling between the two layers forcing the two magnetizations to locally move in synchronicity.

VI. DISCUSSION AND SUMMARY

It is a striking result of our spatially integrating measurements that the quasistatic XMCD measurements show a strong influence of the interlayer exchange coupling while this effect is not observed in the high-frequency FMR data. For the understanding of this effect, it was necessary to study the spatially resolved dynamics covering intermediate frequency scales. These studies revealed different dynamics in different regions of the sample that can be ascribed to a local enhancement of the coupling between both layers due to magnetic stray fields yielding higher coupling in the vicinity of domain boundaries and decoupled dynamics in large domains more distant from the domain walls. Therefore we suggest that the different degree of coupling in the different experiments is related to different magnetodynamic processes occurring in XMCD and FMR measurements.

The discrepancy of the dynamics observed in different regions of the same sample can be used to understand the discrepancy between quasistatic and high-frequency measurements and vice versa; since the high-frequency FMR measurements are carried out in saturation, only a low-angle precession around the effective field axis must be considered. Similar to the spatially resolved dynamics measured in a region far from any domain walls, no considerable coupling between the two layers is observed. The material-dependent behavior is in good agreement with material-selective switching fields H_0 extracted from the XMCD hysteresis loops and damping constants α extracted from the FMR measurements. At the other end of the frequency spectrum, however, the quasistatic

hysteresis loops show matching switching fields and some minor twisting of the NiFe magnetization at lower fields. This behavior corresponds to the observation of a synchronous domain-wall motion in both layers upon field excitation. Thus we can conclude that the quasistatic hysteresis loops are dominated by domain-wall motion.

In summary, we have studied the magnetization dynamics of CoFe/Cr/NiFe trilayers on different time scales. Our experiments revealed a difference in the degree of coupling between the two layers for different time scales studied probed by XMCD, FMR, and PEEM. By carrying out experiments with spatial resolution we have been able to observe the dynamics of different magnetodynamic processes selectively. The analysis of the experimental results showed an almost decoupled magnetization dynamics dominated by

layer-dependent material properties and an enhancement of the coupling near domain boundaries, which could be ascribed to magnetostatic stray field acting there. These findings allowed to understand the observed discrepancy between domain-wall-motion-dominated hysteresis loops and precession-dominated FMR spectra.

ACKNOWLEDGMENTS

This work has been financially supported by the DFG (SFB 491) and the BMBF (05KS7UK1). The authors thank R. Schreiber for the expert sample preparation as well as K. Bickmann, J. Lauer, B. Kuepper, and H. Pfeiffer for technical support. Thanks are due to the ESRF and BESSY beamline staffs for the support during beamtimes.

^{*}Present address: Helmholtz-Zentrum Berlin für Materialien und Energie, Albert-Einstein-Str. 15, DE-12489 Berlin, Germany.

¹J. A. Ewing, Proc. R. Soc. London **38**, 58 (1884).

²M. J. Donahue and D. G. Porter, OOMMF (Object Oriented MicroMagnetic Framework) User's Guide, Version 1.0, Sept. 1999, National Institute of Standards and Technology, Gaithersburg, MD, USA.

³Handbook of Magnetism and Advanced Magnetic Materials, edited by H. Kronmüller and S. S. P. Parkin (Wiley, 2007), Vol. 2.

⁴A. Berger, in *Spintronics, 40th IFF Spring School*, edited by S. Blügel, D. Bürgler, M. Morgenstern, C. M. Schneider, and R. Waser (Forschungszentrum Jülich, 2009).

⁵C. Chappert, A. Fert, and F. Van Dau, Nat. Mater. **6**, 813 (2007).

⁶P. Grünberg, R. Schreiber, Y. Pang, M. B. Brodsky, and H. Sowers, Phys. Rev. Lett. **57**, 2442 (1986).

⁷W. Meiklejohn and C. Bean, Phys. Rev. **102**, 1413 (1956).

⁸J. Nogués and I. K. Schuller, J. Magn. Magn. Mater. **192**, 203 (1999).

⁹G. Schütz, W. Wagner, W. Wilhelm, P. Kienle, R. Zeller, R. Frahm, and G. Materlik, Phys. Rev. Lett. **58**, 737 (1987).

¹⁰G. van der Laan, B. T. Thole, G. A. Sawatzky, J. B. Goedkoop, J. C. Fuggle, J.-M. Esteva, R. Karnatak, J. P. Remeika, and H. A. Dabkowska, Phys. Rev. B 34, 6529 (1986).

¹¹M. Bonfim, G. Ghiringhelli, F. Montaigne, S. Pizzini, N. B. Brookes, F. Petroff, J. Vogel, J. Camarero, and A. Fontaine, Phys. Rev. Lett. **86**, 3646 (2001).

¹²C. M. Schneider and G. Schönhense, Rep. Prog. Phys. **65**, 1785 (2002).

¹³G. Schönhense, H. J. Elmers, S. A. Nepijko, and C. M. Schneider, Adv. Imaging Electron Phys. 142, 159 (2006).

¹⁴H. Stoll *et al.*, Appl. Phys. Lett. **84**, 3328 (2004).

¹⁵M. Farle, Rep. Prog. Phys. **61**, 755 (1998).

¹⁶J. Lindner, K. Baberschke, J. Phys. Condens. Matter 15, R193 (2003).

¹⁷B. Heinrich, *Ultrathin Magnetic Structures II*, edited by B. Heinrich and J. A. C. Bland (Springer, 1994).

¹⁸C. M. Schneider, A. Kaiser, C. Wiemann, C. Tieg, and S. Cramm, J. Electron Spectrosc. Relat. Phenom. **181**, 159 (2010).

¹⁹D. E. Bürgler, C. M. Schmidt, D. M. Schaller, F. Meisinger, R. Hofer, and H.-J. Güntherodt, Phys. Rev. B 56, 4149 (1997).

²⁰D. E. Bürgler, P. Grünberg, S. Demokritov, and M. Johnson, in Handbook of Magnetic Materials Vol. 13, edited by K. H. J. Buschow (Elsevier Science Publishers, Amsterdam, 2001).

²¹A. M. Kaiser, C. Wiemann, S. Cramm, and C. M. Schneider, J. Appl. Phys. **109**, 07D305 (2011).

²²P. Grychtol, R. Adam, A. M. Kaiser, S. Cramm, D. E. Bürgler, and C. M. Schneider, J. Elec. Spect. Rel. Phen. 184, 287 (2011).

²³ FOCUS GmbH, FOCUS IS-PEEM Manual (2001).

²⁴J. Smit and H. G. Beljers, Philips Res. Rep. **10**, 113 (1955).

²⁵J. Krebs, B. Jonker, and G. Prinz, J. Appl. Phys. **61**, 2596 (1987).

²⁶D. Bonnenberg, K. A. Hempel, and H. P. J. Wijn, Magnetic Properties: Alloys between 3d elements: Alloys between Fe, Co or Ni; In: Landolt-Börnstein III/32A (Springer, 1986).

²⁷F. M. Römer *et al*. (unpublished).

²⁸C. M. Schneider, A. Kuksov, A. Krasyuk, A. Oelsner, D. Neeb, S. A. Nepijko, G. Schönhense, J. Morais, I. Mönch, R. Kaltofen, C. D. Nadaï, and N. B. Brookes, Appl. Phys. Lett. 85, 2562 (2004).

²⁹A. Hubert and R. Schäfer, Magnetic Domains: The Analysis of Magnetic Microstructures (Springer, 1998).

³⁰W. D. Doyle, S. Stinnett, C. Dawson, and L. He, J. Magn. Soc. Jpn. 22, 91 (1998).

³¹L. Thomas, M. G. Samant, and S. S. P. Parkin, Phys. Rev. Lett. 84, 1816 (2000).

³²P. J. Metaxas, R. L. Stamps, J.-P. Jamet, J. Ferré, V. Baltz, B. Rodmacq, and P. Politi, Phys. Rev. Lett. **104**, 237206 (2010).